H/A/α-based classification of sea ice using SAR polarimetry

Bernd Scheuchl

Dept. of Electrical and Computer Engineering, University of British Columbia
2356 Main Mall,
Vancouver, B.C.
Canada V6T 1Z4
e-mail: bernds@ece.ubc.ca

Ron Caves

MacDonald Dettwiler and Associates
13800 Commerce Parkway,
Richmond, B.C.
Canada V6V 2J3
e-mail: rcaves@mda.ca

I. Cumming

Dept. of Electrical and Computer Engineering, University of British Columbia
2356 Main Mall,
Vancouver, B.C.
Canada V6T 1Z4
e-mail: ianc@ece.ubc.ca

G. Staples

Radarsat International
13800 Commerce Parkway,
Richmond, B.C.
Canada V6V 2J3
e-mail: gstaples@rsi.ca

Abstract

In anticipation of fully polarimetric SAR data from RADARSAT-2, we use a SIR-C data set to investigate the potential of fully polarimetric spaceborne data for sea ice classification. This paper discusses an entropy/anisotropy/α–angle (H/A/α) classification scheme followed by a minimum-distance classifier based on the complex Wishart distribution of the coherency matrix. Fully polarimetric data acquired by SIR-C over the Labrador Sea off Newfoundland's West Coast is analysed. Data from the two available frequency bands, L- and C-band, are classified separately and the results are compared. Both classifications provide sea ice – open water discrimination and sub-classification of various sea ice types. The main differences between the two results are the number of sea ice classes derived (four for C-band, three for L-band) and the fact that L-band data seems to provide a little better ice/water discrimination. High correlation between the two results with respect to the main feature types (sea ice, water and land) can be noted. Although ground truth is not available, the results are considered of good quality because of the agreement between the L- and C- band results, and consistency with expert human interpretation.

Introduction

Information on the spatial extent of sea ice coverage over time is important for both economic and scientific reasons. Ocean traffic routes and offshore operations at high latitudes are affected by seasonally varying sea ice cover and long term changes in the ice extent are an indicator for climate change.

The importance of sea ice monitoring using Synthetic Aperture Radar (SAR) increased once spaceborne sensors started to provide data on an operational basis. Major advantages are the daylight and cloud coverage independence of the radar as well as the operational coverage of large areas due to satellite technology. Currently, single polarisation sensors such as RADARSAT-1 are successfully in use (Haykin et. al., 1994).

The benefits of radar polarimetry for sea ice classification have previously been demonstrated (Eriksson et. al., 1998), but due to a lack of continuously-available data, it is not used operationally. The second generation of sensors to be launched in the near future will provide multi-polarimetric data. RADARSAT-2 will be the first civilian satellite capable of providing fully polarimetric data (Luscombe et. al., 2001).

Polarimetric data representations

Polarimetric data are a multiple channel measurement thereby providing a more complete inference with natural surface parameters than is possible with a single channel radar system. The coherency matrix **T** is a representation allowing multilooking of the data on a matrix level and is derived by vectorisation of the scattering matrix k_T (Cloude and Pottier, 1996).

$$\mathbf{k}_T = \frac{1}{\sqrt{2}} \begin{vmatrix} \rangle S_{hh} + S_{vv} \langle \\ \rangle S_{hh} - S_{vv} \langle \\ \rangle \quad 2S_{hv} \quad \langle \end{vmatrix}$$

$$\mathbf{T} = k_T \cdot k_T^+$$

where the superscript $^+$ indicates complex conjugation. S_{rt} is the complex scattering amplitude for a given receive (r) or transmit (t) polarisation; h stands for horizontal, v for vertical. Scattering reciprocity is assumed.

Target decomposition

An eigenvalue decomposition of the coherency matrix **T** allows the data to be interpreted in terms of fundamental scattering mechanisms (Cloude and Pottier, 1996). The eigenvalues of **T**, denoted by λ_i, can be seen as the relative strength of the corresponding scattering mechanisms that are represented by the associated eigenvectors. Three parameters, entropy, α angle and anisotropy, are used to characterise the result of the decomposition.

The entropy H represents the randomness of the scattering, H = 0 indicates a single scattering mechanism (isotropic scattering) while H = 1 indicates a random mixture of scattering mechanisms with equal probability and hence a depolarising target:

$$H = \rangle_{i=1}^{3} - P_i \cdot \log_3 P_i \quad \text{where} \quad P_i = \frac{\lambda_i}{\rangle_j \lambda_j}$$

The angle α represents the average dominant scattering mechanism and is calculated from the eigenvectors of **T**. The lower limit is given by surface scattering in the geometrical optics limit (α = 0°) followed by surface scattering under physical optics and the Bragg surface model. Dipole scattering (α = 45°) is followed by double bounce scattering from metallic surfaces and finally dihedral scatter from metallic surfaces (α = 90°), the upper bound. The individual α_i are the scattering mechanisms represented by the three eigenvectors:

$$\alpha = P_1\alpha_1 + P_2\alpha_2 + P_3\alpha_3$$

The anisotropy A represents the relative powers of the second and third scattering mechanisms. A = 0 indicates azimuthal symmetry while values of A > 0 indicate increasing amounts of anisotropic scattering:

$$A = \frac{\lambda_2 - \lambda_3}{\lambda_2 + \lambda_3}$$

These three parameters allow automated classification of the scene by partitioning the H/A/α space. A set of standard thresholds is suggested for this purpose. (Cloude and Pottier, 1997).

The complex Wishart classifier

Using the complex Wishart distribution of the coherency matrix **T**, an appropriate distance measure, d, can then be written according to Bayes maximum likelihood classification as (Lee et. al. 1999):

$$d\left(\langle \mathbf{T} \rangle, \mathbf{V_m}\right) = \ln\left|\mathbf{V_m}\right| + Trace\left(\mathbf{V_m}^{-1}\langle \mathbf{T} \rangle\right)$$

thus leading to a minimum distance classification independent of the number of looks used to form the multilooked coherency matrix $\langle \mathbf{T} \rangle$:

$$d\left(\langle \mathbf{T} \rangle, \mathbf{V_m}\right) \le d\left(\langle \mathbf{T} \rangle, \mathbf{V_j}\right) \quad \text{for all} \quad \omega_j \neq \omega_m$$

A pixel is assigned to a certain class, ω_m, if the distance, d, between pixel and class mean, $\mathbf{V_m}$, is minimum. The scheme is look-independent which allows its application to multi-looked as well as speckle filtered data. An iterative application of the method is possible.

The classification depends upon a training set and was initially developed for supervised classification (Lee et. al. 1994). Using a training set derived without supervision (via target decomposition), makes this combined method a powerful tool for scene classification. The

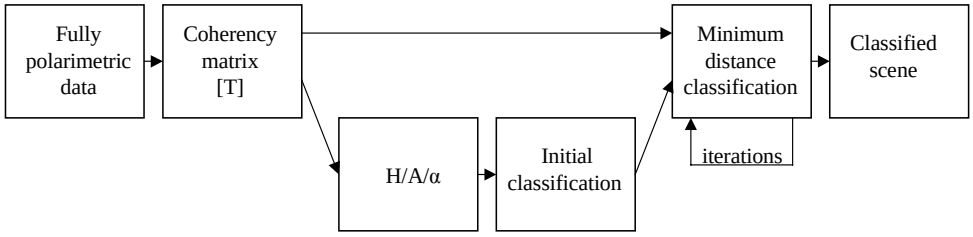

Fig. 1: Combined unsupervised classification.

method as shown in Figure 1 utilises the full polarimetric information and allows look-independent classification. Interpretation of the derived classes and assignment to the various land, water and ice types is a required manual step at the outset, but it may be possible to pre-define the classes after analysis of more data.

SIR-C test data from the Labrador Sea

L- and C-band fully polarimetric data of an area off the coast of Newfoundland were acquired by the first SIR-C mission on April 18, 1994. Figures 2 and 3 show the channel intensities for the two frequencies. The landmass in the upper right of the scene is part of the Gros Morne National Park. Incidence angles range from 26° to 31° (from left to right). Air temperature records for Rocky Harbour (see Figure 8) indicate an average daily temperature above zero degrees for approximately four days prior to data acquisition with the minimum temperature above zero degrees for 24 hours prior to data acquisition.

A photograph taken from the Space Shuttle on April 13 shows the ocean completely covered in ice. However, high temperatures and wind caused significantly different conditions on the acquisition date, which is well into the melt season for this region. Ice in various stages of decline with surface melt and water saturation of snow can therefore be expected. To reduce the effect of speckle noise the data was multilooked so that one pixel covers an area of about 100 m x 100 m (64 looks).

Channel intensities

The C-band channel intensities are shown in Figure 2. The two co-polarised channels show a high variation in backscatter return for open water due to different levels of wind-induced surface roughness. The VV channel is generally stronger than the HH channel in areas of open water. Smooth water shows the weakest return. The sea ice is all first year ice (FYI). A well-defined large floe on the top left of the image shows the strongest return with bright linear structures indicating the presence of ridges or deformed first year ice. The sea ice in the lower half of the image is more chaotic and appears to be seriously affected by surface melt and/or saturated wet snow cover, resulting in a lower backscatter. The cross-polarised channel shows clear separability between sea ice and water at steep incidence angles. Wind features on water are not a factor in this case; however, a differentiation between different sea ice types is not apparent. This channel has potential for ice edge detection in this incidence angle range.

The corresponding L-band channel intensities are given in Figure 4. Several differences can be noted compared to the C-band data. First and foremost, the co-polarised return from areas of open water is not as severely affected by wind induced surface roughness, which is explained by the longer wavelength of the signal. The backscatter coefficient is generally lower, however, the texture of the sea ice correlates well to the C-band data. L-band HH shows good separability of sea ice and water as compared to C-band HH. A higher return for open water in the VV image reduces this capability for this channel.

The HV channel shows the ice edge very well but seems to be more affected by surface melt and/or saturated wet snow cover, which produces a weak return. One big difference with respect to sea ice can be observed in the Bonne Bay area (see Figure 8), the inlet in the upper right part of the

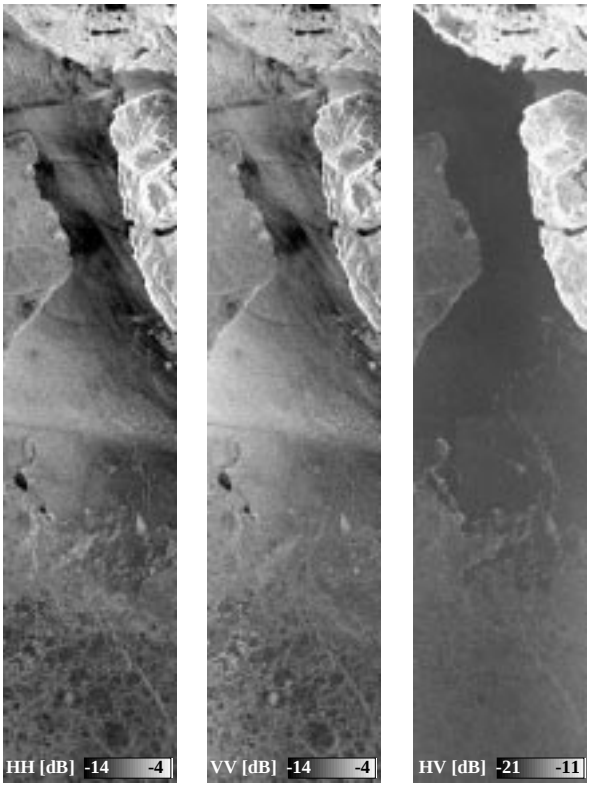

Fig. 2: C-band channel intensities

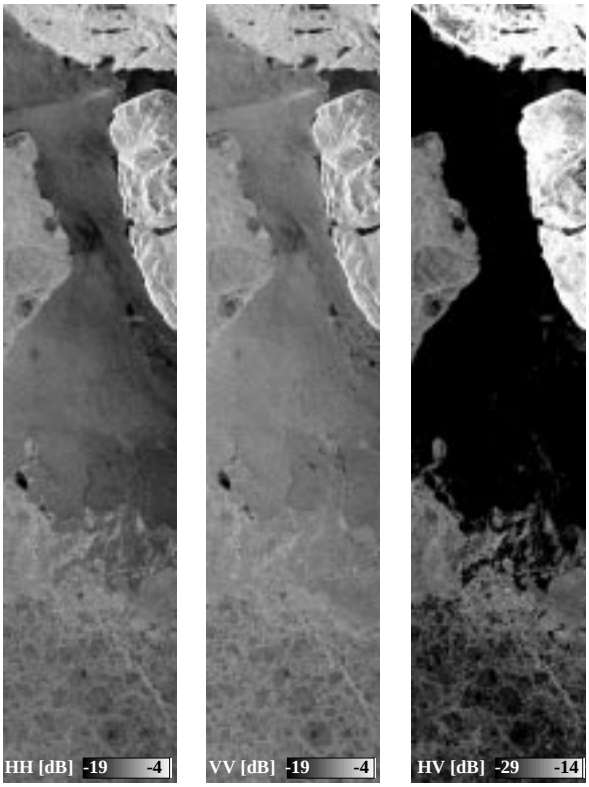

Fig. 3: L-band channel intensities

scene. The inlet appears to be covered by sea ice as can be seen in all channels, except L-band HV.

While all C-band channels show typical sea ice characteristics, the return in the L-band images is extremely weak, which is not the case for the rest of the ice areas in the scene. A similar effect can be seen in the centre of the large floe on the top left of the image. This might be explained by a homogenous ice surface covered by a layer of saturated snow that is rough for a C-band signal but smooth for L-band.

Entropy, Anisotropy and α-angle

Figures 4 and 5 show the target decomposition parameters for the two frequencies. The L-band Entropy H looks very promising for ice/water discrimination, with open water showing lower entropy, whereas wind effects on open water cause the C-band entropy to be ambiguous with respect to ice/water separability.

The scatterplots given in Figures 6 and 7 reveal that L-band entropy covers a wider range of values compared to C-band. The clear separation of land water and sea ice for L-band entropy can also be seen in the Entropy/Anisotropy scatterplot, which shows three distinct clusters. While the C-band Entropy/ Anisotropy scatterplot also shows three distinct clusters related to ice, water and land, the separation is mainly given by the Anisotropy as can be seen in Figure 4. The α angle does contain information about the ground, but type separability is not very good for this parameter.

Dividing the Entropy/Anisotropy/α classification space into 16 partitions as suggested in the literature (Cloude and Pottier, 1997) does not support the clusters just described. The standard partitions are shown by dotted lines in Figures 6 and 7.

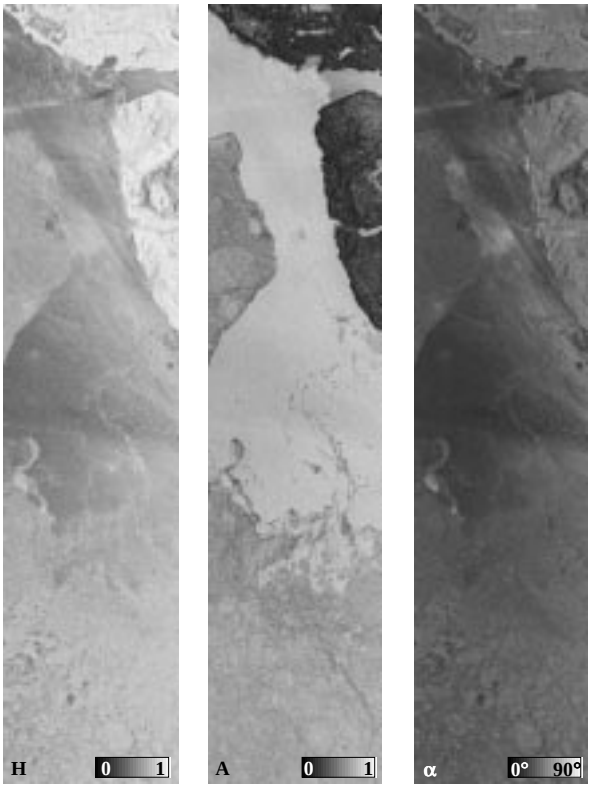

Fig. 4: C-band Entropy, Anisotropy and α–angle

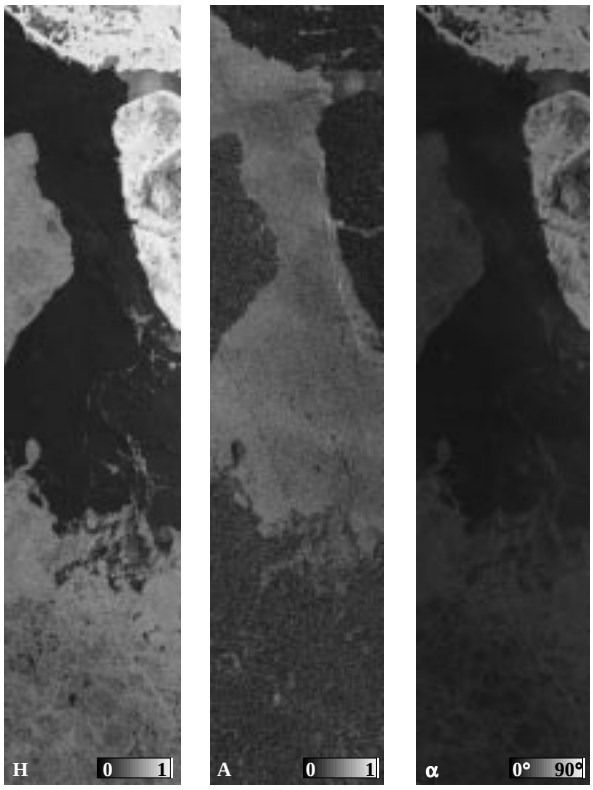

Fig. 5: L-band Entropy, Anisotropy and α–angle

A standardised partitioning scheme has to be used to allow unsupervised classification. With only one data set available, we did not have enough information to change the standard partitions suggested in the literature. However, improvements to the partitions seem possible, based on the observed sea ice classification results. For this data set, for example, the H/A plane seems much more promising for classification purposes than the H/α plane.

Classification results

C-band results of the combined classification for sea ice were first presented by Scheuchl et. al. (2001). The classification results after five iterations of the complex Wishart classifier for C- and L-band are shown in Figure 8. The two frequencies resulted in different numbers of classes, depending on the data distribution in the Entropy/Anisotropy/α classification space. These had to be assigned to main feature types of sea ice, water and land.

A comparison of these three groups for the two frequencies is given in Table 1. The sum of the off-diagonal elements (9.56 % of the total number of pixels) represents the portion of pixels with different classification in L- and C-band. It is mainly sea ice and open water that are confused. Figure 8 shows the results with emphasis on the different sea ice types present. Several land sub-classes (and open water sub-classes for C-band data) were also detected but are not shown here.

A comparison of the different sea ice classes between C- and L-band is difficult, as four classes are derived in C-band vs. three classes in L-band. However, there is some correlation between Sea ice 1 (C-band) and Sea ice A (L-band) as well as between Sea ice 3 (C-band) and Sea ice B (L-band). This is most obvious on the large floe in the top left of the images in Figure 8. These classes represent ice with a rough surface, as the backscatter is strongest (it is likely the oldest and thickest ice in the image, however, no ground truth is available to prove this assumption).

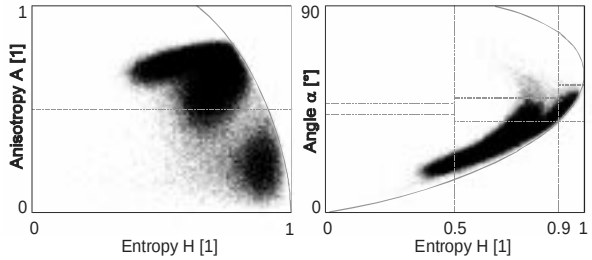

Fig. 6: C-band data distribution in the H/A/α classification space

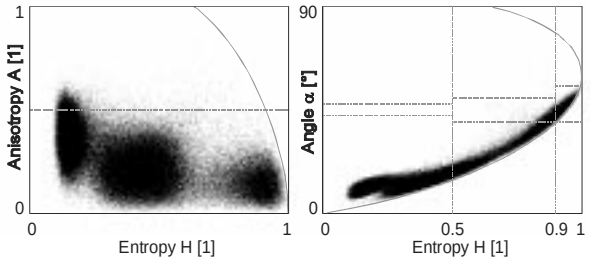

Fig. 7: L-band data distribution in the H/A/α classification space

Polarimetric parameters for the different classes are given in Table 2 for C-band and Table 3 for L band. Sea ice 3 and Sea ice B correlate nicely to brighter areas in the channel intensity images (Figures 2 and 3), thus indicating the presence of ridges.

The lower section of the image is mostly classified as sea ice (types 2 and 4 for C- band and type C for L-band). Areas in this section that were classified as water can best be seen Figure 8. L-band seems to give better separation between saturated snow and open water. Larger areas in this section that are classified as water using L-band data can also be seen in the C-band classification and may well be meltwater ponds.

In general, both frequencies show classification results that are fairly similar. A few more differences should be noted though. Firstly, an area of the large flow in the upper left of the image is classified as water in C-band but not in L-band. The size of the area is unusual as patches of this size are usually classified the same in L- and C-band as in the lower half of the image.

The inlet of Bonne Bay appears to be completely frozen in the C-band classification but not so in the L-band result. One possible explanation is the very low return for this area for L-band thus making the classification vulnerable to noise. On the other hand a small area just left of the inlet is classified as sea ice in L-band but not in C-band. C-band classification generally seems to confuse water and sea ice a bit more. This is also indicated by more ice class pixels in open water.

The lack of ground truth does not allow the comparison of sea ice classes to actual sea ice types at this time. However, the spatial structure of the ice types, the correlation to backscatter strength as well as agreement of the results with expert human interpretation indicates that this automated classification scheme works well.

The C- band polarimetric parameters for the class means are summarised in Table 2. Land classes show generally a stronger return as compared to sea ice and water. Water shows high variability depending on wind-induced surface roughness. Three parameters, the cross-polarised channel intensity HV, the Anisotropy A and the co-polarised ratio HH/VV, can be identified as providing the best separation of the main feature types, sea ice, water and land. The cross-polarised channel intensity is lowest for water and highest for land. All three water classes show the same average HV, probably as the low return is close to the system noise level. This would explain why wind-affected water surfaces do not have any effect on this channel. The Anisotropy A is highest for water and lowest for land. The co-polarised ratio HH/VV is positive for land, between 0 dB and –0.6 dB for sea ice and approximately –1 dB for water. The other parameters do not uniquely identify a certain feature type.

The L- band polarimetric parameters for the class means are summarised in Table 3. L-band shows generally better separability of the main feature types. The Entropy is certainly the single most promising parameter as can be seen in Figures 5 and 7. The reduced sensitivity to wind-induced water surface roughness is the main reason for the improved capability to distinguish between sea ice and water. The automated classification leads to six land classes compared to four land classes for the classification using C-band.

The availability of a more representative data set, i.e. data available on an operational basis, would certainly allow further reduction of required user interaction as class means could be compared to class libraries representing different land, ice and water types.

Conclusions

Fully polarimetric SAR data show a strong capability for unsupervised sea ice classification. A combined Entropy/Anisotropy/α classification followed by a complex Wishart classifier (five iterations) was used. Class assignment to the main types of sea ice, water and land is a required manual step for the time being. Results from C-band and L-band data are compared and the three main class types show high correlation between the two results. Sub-classes within the main types were not compared as different numbers of sub-classes were derived for the two frequencies.

Further algorithm improvement seems possible, as the Entropy/Anisotropy plane is promising for a separation of the land, sea ice and open water classes, and a modified partitioning of the features used in the primary classifier are expected to lead to an improved result. A more representative data set with ground truth available would be required to investigate this option.

Acknowledgements

This work was performed under contract to the Canadian Space Agency (No. 9F028-0-4902/06) as part of the Earth Observation Applications Development Program. The authors thank Dean Flett from the Canadian Ice Service (CIS) for his valuable comments, and Environment Canada and NASA/JPL for providing data.

References

Cloude S. R. and E. Pottier. (1996). "A review of target decomposition theorems in radar polarimetry," *IEEE Trans. Geosci. Remote Sensing*, vol. 34, no. 2, pp. 498-518.

Cloude S. R. and E. Pottier. (1997). "An Entropy Based Classification Scheme for Land Applications of Polarimetric SAR," *IEEE Trans. Geosci. Remote Sensing*, vol. 35, no. 1, pp. 68-78.

Eriksson L., M. Drinkwater, B. Holt. E. Valjavek and O. Nortier. (1998). "SIR-C Polarimetric Radar Results from the Weddell Sea, Antarctica," *Proc. IGARSS'98*, Seattle, USA.

Haykin S., E. O. Lews, R. K. Raney and J. R. Rossiter. (1994). *Remote Sensing of Sea Ice and Icebergs*, Wiley.

Lee J.-S., M. Grunes and R. Kwok. (1994). "Classification of multi-look polarimetric SAR imagery based on complex Wishart distribution," *Int. J. Remote Sensing*, vol. 15, no. 11, pp. 2299-2311.

Luscombe A., A.A. Thompson, K. James and P. Fox. (2001). "New modes and techniques of the RADARSAT-2 SAR," *Proc. IGARSS'01*, Sydney, Australia.

Pottier E. and J.-S. Lee. (1999). "Application of the H/A/α Polarimetric Decomposition Theorem for Unsupervised Classification of Fully Polarimetric SAR Data Based on the Wishart Distribution," in *Proc. CEOS'99*, Toulouse, France.

Scheuchl B., R. Caves, I. Cumming and G. Staples. (2001). "Automated Sea Ice Classification Using Spaceborne Polarimetric SAR data," *Proc. IGARSS'01*, Sydney, Australia.

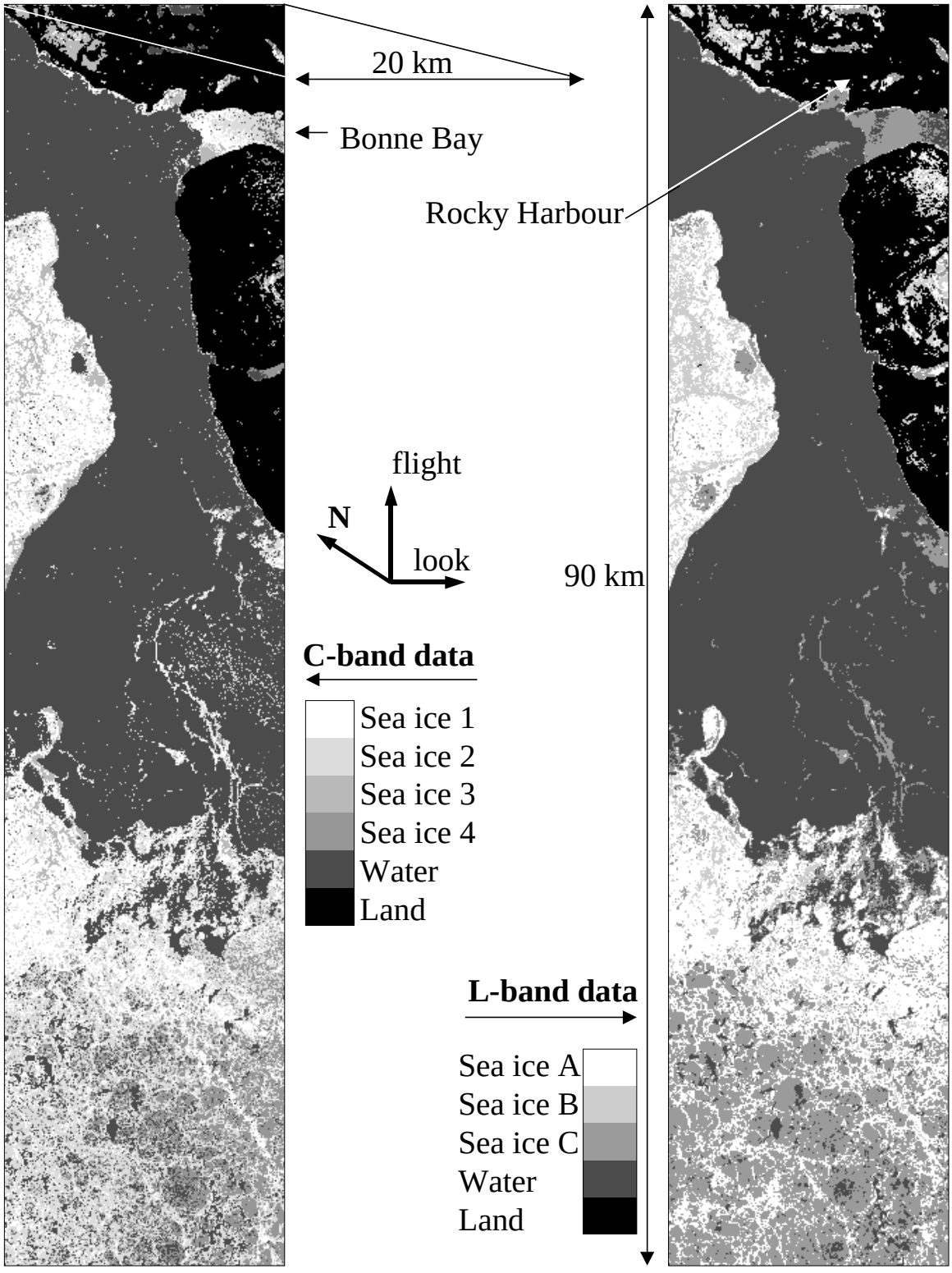

Fig. 8: C-band (left) and L-band (right) classification results. Water is shown in dark grey and land is shown in black, while various types of sea ice are shown in lighter shades.

Table 1: C-band and L-band classification results for the main class types. The "Confusion Matrix" shows the percent of pixels assigned to one class in a given band, but another class in the other band.

			C-band		
			Land	**Sea ice**	**Water**
		(total)	**(13.45)**	**(41.04)**	**(45.51)**
L-band	**Land**	**(11.99)**	11.65	0.31	0.03
	Sea ice	**(44.77)**	1.78	38.15	4.84
	Water	**(43.24)**	0.02	2.58	40.64

Table 2: Average C-band polarimetric parameters for the derived classes

Ice Type	HH	HV	VV	ρ_{hhvv}	ρ_{hvvv}	HH/VV	HV/VV	H	A	α
	dB	dB	dB	-	-	dB	dB	-	-	degrees
Sea ice 1	-8.9	-16.9	-8.7	0.65	0.25	-0.2	-8.2	0.68	0.54	29.0
Sea ice 2	-10.3	-17.1	-9.4	0.60	0.30	-0.5	-7.4	0.72	0.62	32.0
Sea ice 3	-7.4	-16.2	-7.3	0.69	0.19	0.0	-8.9	0.65	0.44	26.9
Sea ice 4	-11.6	-17.3	-11.0	0.50	0.36	-0.6	-6.3	0.77	0.67	37.9
Water 1	-12.7	-17.9	-11.5	0.50	0.40	-1.2	-16.4	0.74	0.77	38.8
Water 2	-10.7	-17.9	-9.7	0.68	0.32	-0.9	-8.2	0.64	0.74	28.4
Water 3	-8.5	-17.9	-7.5	0.79	0.25	-0.9	-10.4	0.51	0.69	21.7
Land 1	-0.5	-8.8	-1.4	0.67	0.05	0.9	-7.4	0.72	0.07	27.6
Land 2	-4.8	-11.3	-5.6	0.52	0.09	0.8	-5.7	0.85	0.15	36.6
Land 3	-6.7	-12.6	-7.5	0.45	0.14	0.8	-5.1	0.88	0.21	40.4
Land 4	-8.7	-14.0	-9.3	0.38	0.20	0.6	-4.6	0.91	0.31	44.0

Table 3: Average L-band polarimetric parameters for the derived classes

Ice Type	HH	HV	VV	ρ_{hhvv}	ρ_{hvvv}	HH/VV	HV/VV	H	A	α
	dB	dB	dB	-	-	dB	dB	-	-	degrees
Sea ice A	-12.2	-24.0	-11.6	0.83	0.07	-0.6	-12.4	0.45	0.17	14.4
Sea ice B	-10.4	-21.6	-10.1	0.80	0.06	-0.3	-11.5	0.50	0.16	15.7
Sea ice C	-13.9	-27.2	-12.8	0.88	0.08	-1.1	-14.4	0.35	0.20	12.2
Water	-14.0	-32.0	-12.0	0.95	0.17	-2.0	-20.0	0.16	0.37	10.2
Land A	-10.9	-17.3	-10.8	0.51	0.03	-0.1	-6.5	0.85	0.04	35.1
Land B	-8.9	-14.8	-9.3	0.44	0.02	0.3	-5.5	0.89	0.03	39.9
Land C	-7.2	-13.2	-7.8	0.44	0.02	0.6	-5.4	0.89	0.03	40.8
Land D	-1.0	-9.3	-0.9	0.70	0.05	-0.1	-8.4	0.68	0.02	24.5
Land E	-5.2	-11.8	-5.5	0.52	0.03	0.3	-6.3	0.85	0.03	35.9
Land F	-7.6	-17.5	-7.4	0.78	0.05	-0.3	-10.1	0.56	0.05	18.3